

Molecular Dynamics Simulation of FCC Metallic Nanowires: A Review

JIJUN LAO,^{1,2} MEHDI NAGHDI TAM,¹ DINESH PINISETTY,¹
and NIKHIL GUPTA¹

1.—Department of Mechanical and Aerospace Engineering, Polytechnic Institute of New York University, Brooklyn, NY, USA. 2.—e-mail: jlao@poly.edu

Molecular dynamic simulation studies are reviewed to understand the influence of strain rate, temperature, and cross-section size on the mechanical properties of face-centered cubic (FCC) metallic nanowires (MNWs). The yield stress of FCC MNWs is found to be 100 times higher than that of the corresponding bulk metals. The yield strain and fracture stress of MNWs are also found to be significantly higher compared with those of the bulk metals. The influence of deformation mechanisms (slip and twinning) on the mechanical properties of FCC MNWs is discussed. FCC MNWs are found to exhibit novel structural reorientation, phase transformation, elastic recovery, pseudoelasticity, and shape memory effect. MNWs with body-centered cubic (BCC) and hexagonal closed-packed crystal structures are compared with the FCC MNWs. Pseudoelasticity was also observed in BCC MNWs similar to that of FCC MNWs. Dense nano-twin arrays were found in Mg nanowires despite the high twin boundary energy.

INTRODUCTION

Nanowires are considered one-dimensional (1D) structures that have drawn a great deal of interest as a result of their remarkable physical, mechanical, electronic, optical, and magnetic properties.^{1–3} The unique properties of nanowires compared with their bulk counterparts can be attributed to their large surface-area-to-volume ratio.⁴ The behavior of surface atoms differs from those inside the bulk because the surface atoms have a coordination number deficiency and are subjected to surface stresses.^{5,6} The surface stresses vary based on the nanowire material and crystal structure. For example, surface stresses in face-centered cubic (FCC) metals are typically tensile,⁷ leading to the contraction of nanowires, whereas surface stresses in semiconductor nanowires are typically compressive, leading to an increase in length of semiconductor nanowires.⁸

Metallic nanowires (MNWs) have been given extensive attention in recent years as a result of their widespread applications in myriad areas such as optoelectronic applications,⁹ nano-electronic and nanomechanical devices,¹⁰ catalysis, nanopipette probes, superconductors, and reinforcement in high-strength/

light-weight composite materials.^{11–16} They have also been explored as tips for scanning tunneling and atomic force microscopes.¹⁷ MNWs are attracting interest as a result of their significantly higher yield strengths and modulus compared with the bulk metals.

Molecular dynamics (MD) simulation has become an invaluable technique to study a variety of complex physical, chemical, and biochemical systems. The ability of MD to build observations across length scales based on the data at atomic level has enhanced its spectrum of applications. MD techniques have been applied to analyze structural and dynamical response of polymers,^{18–21} drug delivery and diffusion of small molecules through biological membranes,^{22–26} physical properties of nanowires,^{4,27–30} and properties of nanocomposites.^{31–35} In the present work, the results of MD simulations on FCC MNWs are summarized.

Recent MD studies have identified two distinct mechanisms that mediate the structural response in FCC MNWs: novel phase transformations³⁶ and lattice reorientation.³⁷ Associated with reversibility and temperature dependence of these structural changes, pseudoelastic behavior and shape memory effect (SME) are also discovered.^{38–41} The following

sections discuss MD simulation methodology, properties of FCC nanowires, and comparison of their properties with body-centered cubic (BCC) and hexagonal closed-packed (HCP) nanowires.

MD SIMULATION METHODOLOGY

MD is a simulation technique where the time evolution of a set of interacting atoms is followed by integrating their equation of motion. It consists of integrating Newton's second law for each atom present in the system by discretization of time. In general, it is difficult to obtain an analytical solution that precisely describes the atoms' trajectories. Therefore, the equations of motion are solved numerically using a time-discretized finite difference methodology such as the Verlet method or the velocity Verlet method, which incorporate the velocities explicitly into the integration scheme.⁴² The initial atomic positions for metallic systems are defined on the crystal lattice of the metal, while the initial velocities are assigned according to the Boltzmann distribution at the given simulation temperature.

The validity and accuracy of MD simulation results depend on the accuracy of the interatomic forces used as inputs, which rely on the selection of an efficient underlying interatomic force-field potential. For modeling metallic systems, the most commonly used potential is the semi-empirical embedded atom method (EAM) potential. The parameters of EAM potential are generally obtained by fitting cohesive energy, equilibrium lattice constant, elastic constants, unrelaxed vacancy formation energy, bond length, and diatomic bond strength. Since its introduction, the ability and viability of EAM in modeling metals have been extensively analyzed and tested.⁴³ The classic EAM method is not suitable for describing systems in which covalent bonds are present,⁴⁴ such as carbon (in diamond or graphite structures), because the EAM description does not account for the angular dependence of the interatomic interactions. To account for angular dependence, as in the case of the BCC lattice where it is important, a modified embedded atom method (MEAM) was proposed.⁴⁵ The total energy U in a system of N atoms in the EAM framework can be written as

$$U = \sum_i^N \left(F_i(\bar{\rho}_i) + \frac{1}{2} \sum_{j \neq i}^N \varphi_{ij}(R_{ij}) \right) \quad (1)$$

where φ_{ij} is the pairwise interaction term corresponding to the electrostatic interaction between atoms i and j , R_{ij} is the interatomic distance between atoms i and j , and F_i is the embedding term describing the quantum effects and is a function of the local electron density. The embedding term can be considered the energy required to embed an atom into an electron gas with a density ρ_i . This includes the contribution of electron density that is the key to

EAM and provides a many-body contribution to the energy. ρ_i , the electron density term, depends on the distance between two atoms.

A model for nanowires is usually extracted from bulk crystal according to the desired crystalline orientation, a method that is similar to the top-down fabrication process. The initial velocities are assigned according to the Boltzmann distribution at the given simulation temperature. Then a relaxation process is performed to allow the system to reach an equilibrium state corresponding to the minimum energy state at the simulation temperature, and then finally the tension/compression test can be conducted.

MECHANICAL PROPERTIES OF FCC MNWS

The nanowires with FCC crystal structure are widely studied.^{46–51} This is because the FCC structure is a common crystal structure for a large number of metals and their potentials are well developed, which is crucial to conduct MD simulations. The mechanical properties and deformation modes are discussed in this section.

Yield Strength

Most of the current MD simulations are focused on nanowires with less than 10 nm diameter because of computational limitations. Table I shows the yield strength values obtained from MD simulation for FCC MNWs. The yield strength of FCC MNWs can be 100 times higher than the corresponding bulk materials.⁵² MD studies have been applied extensively to predict the influence of a large number of variables including size, strain rate, crystalline orientation, and temperature on the mechanical properties of MNWs. A representation of FCC MNW with square and circular cross sections is shown in Fig. 1. The axial direction, side surfaces, and width for square and diameter for circular cross-sectioned nanowire are marked in Fig. 1. MD simulation results focused on the effect of yield strength as a result of the variation in strain rate, temperature, and cross section of nanowire are discussed in the following sections.

Effect of Strain Rate

Mechanical properties of FCC MNWs are found to be dependent on the strain rate.^{53–56} Available computational resources can conduct studies in the 10^7 – 10^{11} s^{-1} strain rate range, where the yield strength and yield strains are found to increase with strain rates.

The effect of strain rate on the yield strength of nickel (Ni) nanowire of 2.53 nm width is depicted in Fig. 2a. The yield strength value at a strain rate of 10^8 s^{-1} is found to be 7.98 GPa, but the yield strength at a higher strain rate of $1.4 \times 10^{11} \text{ s}^{-1}$ is found to be 11.3 GPa, which is a 40% increase.⁵⁷ The dependence of yield stress on the strain rate is

Table I. Yield strength of commonly studied FCC metal nanowires obtained by MD simulations.

Metal	Orientation (axial/side surfaces)	Wire size ^a (nm)	Simulation temperature (K)	Yield strength (GPa)	References
Au	$\langle 100 \rangle / \{110\}$	2.45	2	4.2	47
	$\langle 110 \rangle / \{110\} \{001\}$	2.45	50	4.3	51
Cu	$\langle 100 \rangle / \{110\}$	1.96	300	4.9	89
	$\langle 110 \rangle / \{111\}$	1.52	300	6.52	50
Ni	$\langle 100 \rangle / \{100\}$	2.53	300	8.3	57
	$\langle 110 \rangle / \{110\} \{001\}$	2.1	300	14.26	90
Pd	$\langle 100 \rangle / \{100\}$	1.78	100	7.5	38
	$\langle 110 \rangle / \{111\}$	2.57	100	6.1	38

^aSize refers to width or diameter in square or circular cross-section MNWs, respectively.

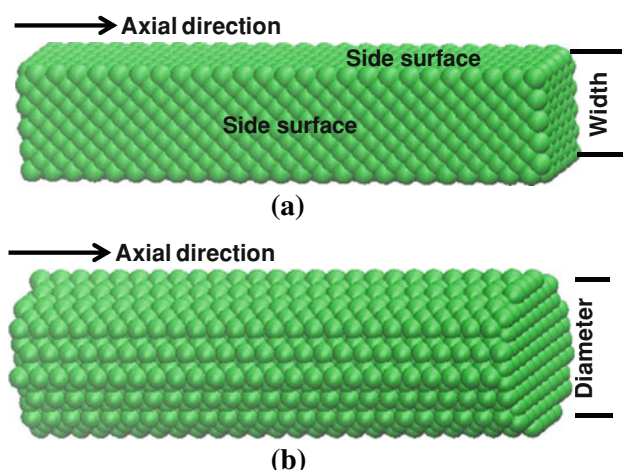


Fig. 1. Representation of FCC nanowire with (a) square cross section with side surface and (b) circular cross section.

believed to be associated with a dynamic wave effect,⁵⁴ which inhibits the dislocation initiation or occurrence of slip in MNWs. It can also be noted that the yield strength of nanowire is significantly higher than the experimental value for bulk Ni, which is 0.14 GPa. However, direct comparison of the values might not be appropriate because the nanowire model in MD was defect free, whereas bulk Ni has defects such as dislocations, voids, and impurities.⁵⁷

Apart from the effect of strain rate, the nanowire size also has a significant influence on the yield strength. The yield strength of platinum (Pt) nanowire as a function of strain rate and the size of the nanowire is shown in Fig. 2b. It is found that at a higher strain rate of $4 \times 10^{10} \text{ s}^{-1}$, the yield strength increases by 23% when the diameter of the nanowire is decreased from 5.88 nm to 1.96 nm. It can also be seen that for any nanowire diameter, the yield strength increases with strain rate except for the nanowire with a diameter of 5.88 nm, which corroborates well with results shown for Ni nanowires (Fig. 2a).

Apart from strain rate and size, the cross-sectional shape was also found to have an influence over the yield strength of the nanowire. The yield strength of

the gold (Au) nanowire as a function of strain rate and cross-section size is shown in Fig. 2c for square (below dashed line) and circular (above dashed line) cross sections. The legend in this figure represents the cross-section size of the MNW. It is found that the yield strength is higher for nanowires with a circular cross section when compared with that of the square cross section. Also, except for the highest strain rate, $3 \times 10^{10} \text{ s}^{-1}$, the yield strength increases with the strain rate for any diameter of the nanowire. This result corroborates well with those reported for Ni and Pt nanowires (Fig. 2a, b). This exception at the highest strain rate can be attributed to the nonlinearity of stress-strain response resulting from the constrained dynamic free vibration.⁴⁹ The increase in the yield strain with strain rate indicates a strain hardening mechanism in MNWs.⁵⁷ The cases with strain rates below 10^6 s^{-1} are not readily available; yet they may be studied as the available computational power increases.

Effect of Temperature

The dependence of mechanical properties on simulation temperature has also been studied.^{55,58–60} The yield strength decreases with increasing temperature, and the reduction can be as much as 77% when temperature rises from 1 K to 600 K for copper nanowire with a square cross section as shown in Fig. 3.⁶⁰ A low yield strength of MNWs at high temperature is because the thermal fluctuations facilitate overcoming the energy barrier for dislocation nucleation.

Effect of Nanowire Size

The deformation behavior and mechanical properties of MNWs are strongly dependent on the cross-sectional size, namely, the nanowire width. It is found that the MNWs with a smaller cross section are stronger if the wires preserve their crystal structure during the deformation. As shown in Fig. 4, the yield strength of [100] Au nanowire with a square cross section increased from 4.0 to 4.4 GPa when the width of wire is reduced from 6 nm to 1.4 nm.⁴⁷ This result also corroborates well with the

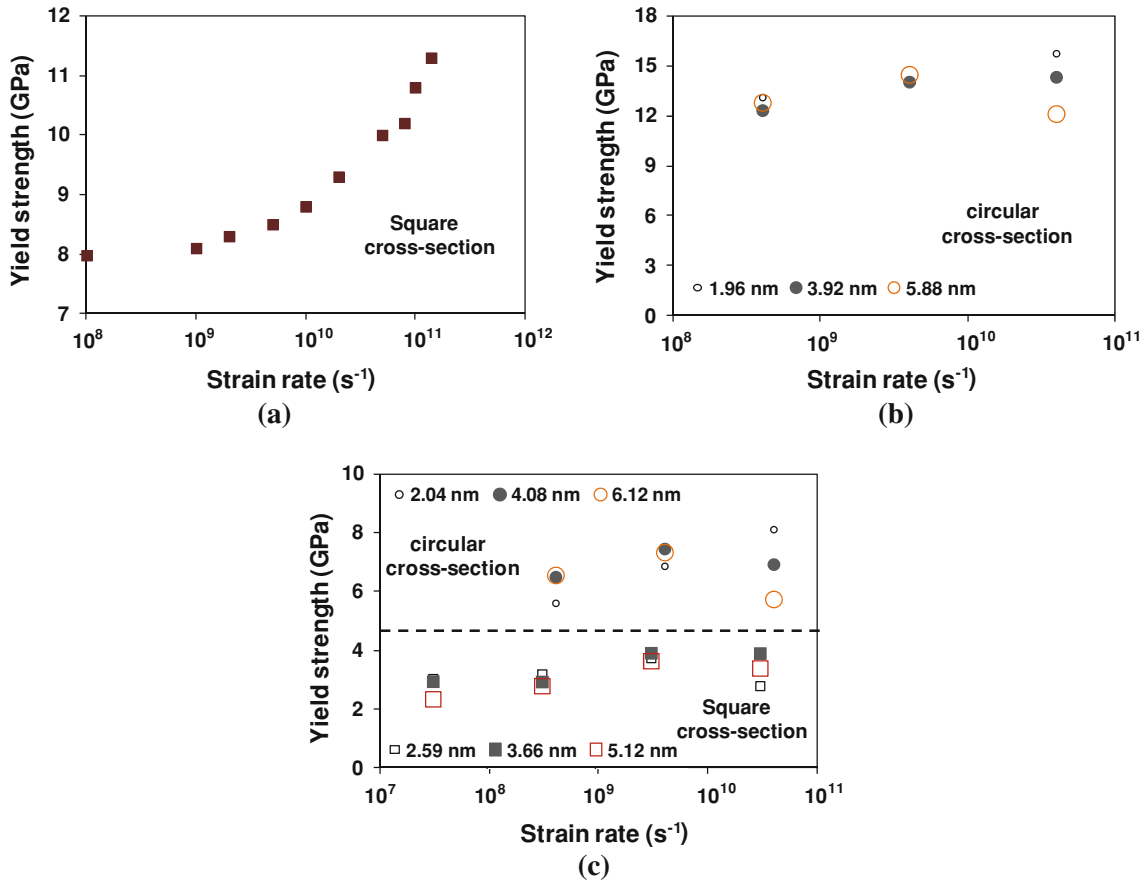


Fig. 2. Effect of strain rate on yield strength of MNWs (a) Ni,⁵⁷ (b) Pt,⁴⁹ and (c) Au with square cross section⁵⁵ (below dashed line) and circular cross section⁵⁶ (above dashed line).

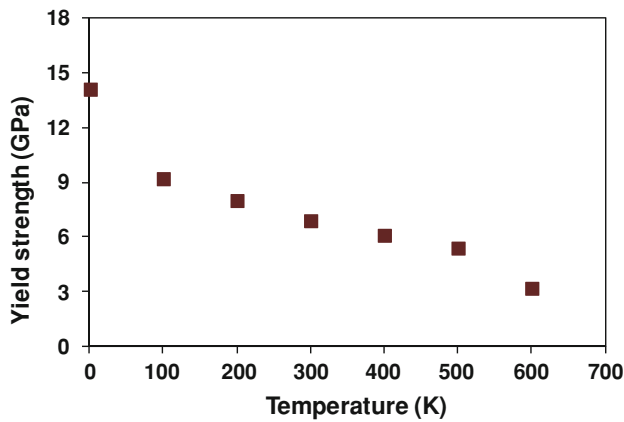


Fig. 3. Effect of temperature on yield strength of Cu nanowires.⁶⁰

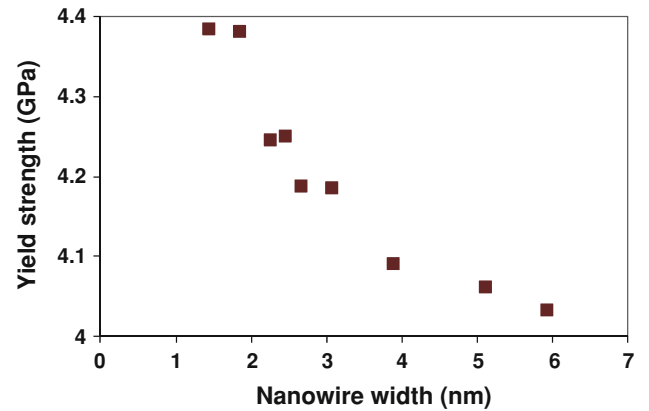


Fig. 4. Effect of wire cross-section width on yield strength of Au nanowires.⁴⁷

yield strength data for Au and Pt nanowires presented in Fig. 2b, c. This phenomenon can be understood by noticing that in wires with larger cross-sectional areas, there is an enhanced opportunity for dislocation motion, which leads to a decrease in both yield strain⁵⁵ and yield stress.^{48,52,54} Besides the width of nanowire, the crystallographic orientation also has an

important influence on mechanical properties (refer to Table I).

Deformation Mechanism: Slip or Twinning

Understanding the fundamentals of deformation mechanisms of MNWs is important to predict

accurately the mechanical properties of MNWs. Both slip and twinning have been observed in the MD simulation of MNWs. Figure 5 shows an example of (a) slip and (b) twinning occurring during the deformation of FCC MNWs. The slip planes and twin boundaries can be identified in the wire based on localized atomic geometry. However, when compared with the plastic deformation of bulk metals, determination of dominant mechanism is quite different and more complicated in MNWs. This is because, first, slip itself in MNWs can be conducted by either perfect (full) dislocations or partial dislocations; second, it is found that the competition between slip and twinning is not only dependent on the loading type and temperature, but also it is strongly affected by the geometric factors of wires. These factors include the cross-sectional size and crystallographic orientation in the axial direction and on the side surfaces.^{51,61}

By performing the mechanical deformation on Cu, Ni, Au, and Al using MD simulation, Liang and Zhou³⁹ reported that the competition between partial dislocation slip and twinning is material dependent. For $\langle 110 \rangle$ axial orientation and $\{111\}$ side surfaces, Cu and Ni MNWs deform by twinning under tensile loading, Al wires deform by full dislocation slip, and Au wires deform by twinning at low simulation temperature (5 K) and by partial dislocation slip at high temperature (200 K).³⁹ This result can be explained well by ranking the materials' ability to twin using a twinnability factor based on the theory developed by Tadmor and Bernstein,⁶² which quantifies the competition between slip and twinning. The twinnability factor depends on the measure of energy barriers associated with

twinning and slip. This factor is a function of stable stacking fault energy γ_{sf} , unstable stacking fault energies γ_{us} , and unstable twinning energy γ_{ut} . These quantities can be calculated from a generalized stacking fault energy (GSFE) curve that represents the continuous energy cost of rigidly shifting two semi-infinite blocks of crystals. γ_{us} is defined as the maximum value on the GSFE curve; γ_{sf} is taken as the local minimum between two γ_{us} peaks; and γ_{ut} characterizes the energy barrier for creating a nanotwin by shifting a layer adjacent to an existing intrinsic stacking fault. The twinnability factors calculated for Cu, Ni, Au, and Al are 0.896, 0.878, 0.828, and 0.788, respectively.³⁹ The twinning mechanism is favored with a higher twinnability factor, whereas slip is favored with a lower twinnability factor. The values of this factor suggest that twinning is most favorable in Cu and least favorable in Al. This prediction also corroborates well with MD simulations.³⁹

Although the twinnability factor ranks the FCC metals in terms of their tendency to twin, this factor is only designed to distinguish between twinning and full dislocation slip. It is not effective to select the dominant deformation mechanism if partial dislocation slip is involved.^{39,50,61} Weinberger and Cai⁶³ proposed a two-parameter criterion based on both the Schmid factor (being purely geometric in nature without the influence of metallic properties) and GSFEs. Depending on the relative magnitudes of the two parameters, this model divides the parameter space into three domains, which correspond to full dislocation slip, partial dislocation slip, and twinning. The model predicts that twinning is always favored over partial dislocation slip as long as full dislocation is not dominant mechanism,

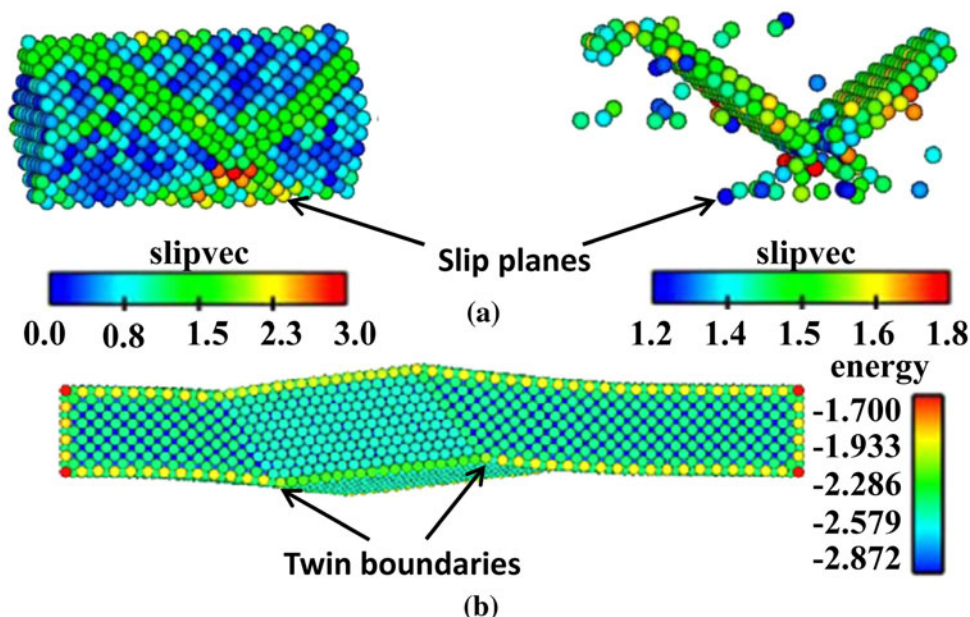


Fig. 5. (a) Slip during the yielding of Au nanowire (left snapshot shows all atoms, and right one shows only atoms on the slip planes).⁴⁷ Atoms are colored according to the magnitude of the slip vector. (b) Twinning during deformation of Ag nanowires⁶⁷ (atoms are colored according to the magnitude of the potential energy) (Color figure online).

which is not consistent with all MD simulations. However, model predictions might still be valid and consistent with MD simulations at high strain rates wherein the boundary between twinning and partial dislocation slip will be shifted. Moreover, the boundary between these two mechanisms is not abrupt because both twinning and partial dislocation slip occur through the stochastic event of dislocation nucleation.

Structural Reorientation and Phase Transformation

Recent MD simulation studies have identified two novel features in FCC MNWs. In certain metals when the cross-sectional area is below 4 nm^2 , the surface stress can be large enough to cause a phase transformation that drives the system from the initial FCC structure into a body-centered tetragonal (BCT) structure^{36,64–66} (see Fig. 6a). This phase transformation is driven primarily by the surface stresses and allows a reduction of the wire surface energy. This phenomenon observed by MD simulation is an intrinsic nanoscale phenomenon and does not occur in wires of macroscopic diameters because surface effects are size dependent and are substantial only at such a small scale.^{36,47} For nanowires with larger cross-sectional areas, the same surface stress can also lead to other structural transformation mechanisms such as crystal structure reorientation. It was found that FCC wires with a cross-sectional area of 6.6 nm^2 having an initial $\langle 100 \rangle$ orientation with $\{100\}$ side surfaces can reorient spontaneously under the effect of surface stress into $\langle 110 \rangle$ orientations with $\{111\}$ side surfaces³⁷ (see Fig. 6b). MD simulations have been performed to study this phenomenon by various research groups.^{37,38,40,41,51,67,68} The existence of both phase transformation and structural reorientation phenomena have been confirmed by density functional theory calculations.⁶⁵

The stress–strain curves (Fig. 7) correspond to the two behaviors presented in Fig. 6. Comparison

of the two stress–strain curves in Fig. 7 indicates that there are both similarities and differences between the two systems. Although both transformations can achieve similar levels of strains, they differ qualitatively and quantitatively in the plateau regions (between points B and C). While the loading stress–strain curve for the lattice reorientation controlled behavior exhibits a small strain hardening over the range of strains delimited by the beginning (point B) and the end stage (point C) of the reorientation process (see Fig. 7b), no such phenomena is observed on the corresponding portion of the stress–strain curve for the FCC-to-BCT phase transformation (see Fig. 7a). Moreover, although in both mechanisms the deformations are fully recovered when the stress is reduced to zero, there are major differences between the two stress–strain curves during the unloading stage. For the FCC-to-BCT phase transformation, the loading and the unloading stress–strain curves follow almost the same path (see Fig. 7a, point B–C), whereas for the lattice reorientation, the loading and unloading paths form a well-defined hysteresis loop (see Fig. 7b). The reversible FCC-to-BCT phase transformation is mediated by short-range atomic rearrangements, similar to those found in austenite-to-martensite phase transformations, and it does not involve nucleation and propagation over large distances of any structural defects. In contrast, in the lattice reorientation, both strain hardening and hysteresis loop observed are the products of repetitive nucleation, glide, and annihilation of Shockley partial dislocations.

Pseudoelasticity and Shape Memory Effect

A schematic of the pseudoelasticity behavior and SME caused by lattice reorientation of nanowire is shown in Fig. 8. Specifically, the nanowire with $\langle 110 \rangle$ in longitudinal direction and $\{111\}$ side surfaces ($\langle 110 \rangle/\{111\}$) can reorient to a $\langle 100 \rangle/\{100\}$ nanowire upon external loading. During the unloading step, if the temperature rises to a certain value, there will be a reorientation back to

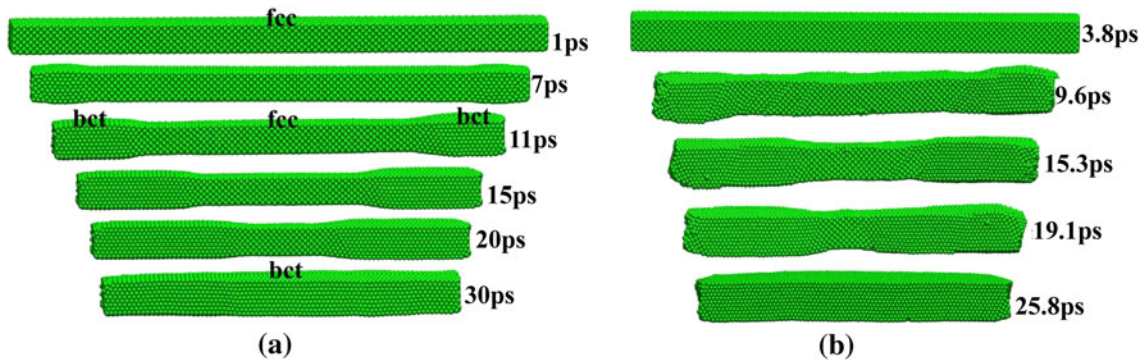


Fig. 6. (a) Snapshots depicting the time evolution of a 1.78×1.78 -nm palladium (Pd) nanowire during the spontaneous, surface-stress-driven, FCC-to-BCT phase transformation at constant temperature of 100 K. (b) Snapshots depicting the dynamic progression of spontaneous crystalline reorientation at 300 K in a Pd nanowire of 2.57×2.57 -nm cross-sectional area.³⁸

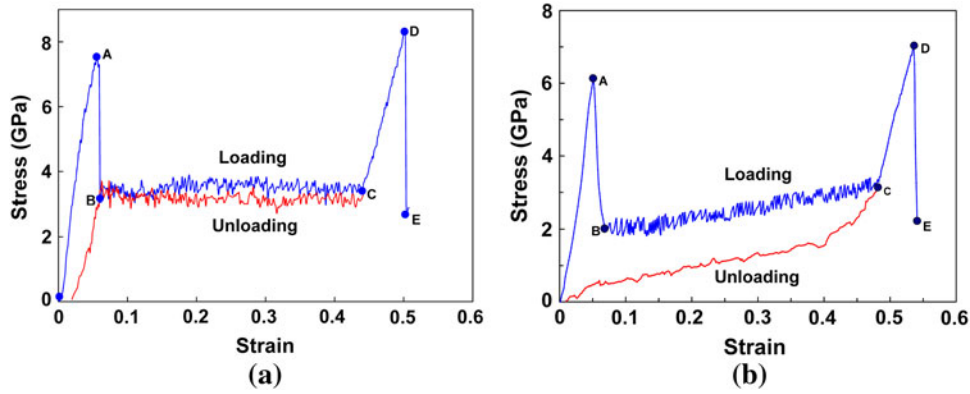


Fig. 7. (a) Stress–strain curve for the 1.78×1.78 -nm Pd cross-section nanowire during loading and unloading at 100 K. Curves between B and C correspond to the FCC-to-BCT phase transformation. (b) The stress–strain curve of a 2.57×2.57 -nm cross-section Pd nanowire during loading and unloading at 300 K. The linear portion of curve, between points B and C, corresponds to the sample elongation caused by the steady advance of the lattice reorientation from the ends toward the center of the nanowire.³⁸

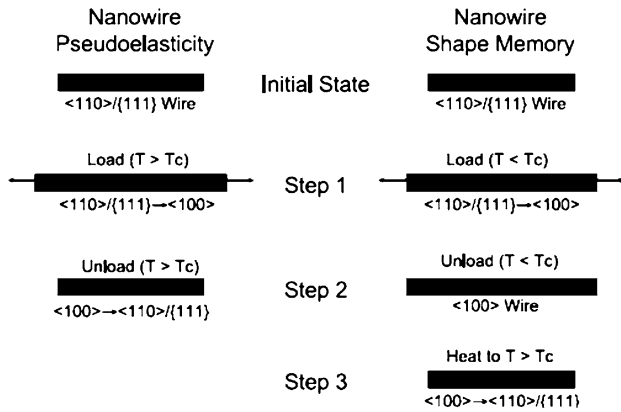


Fig. 8. Schematic of pseudoelasticity and SME in FCC MNWs. T_c is the critical temperature for an initially $\langle 100 \rangle$ wire to reorient to a $\langle 110 \rangle$ wire for a given wire cross section.⁶⁷

$\langle 110 \rangle / [111]$ configuration with low energy. This temperature is usually defined as the critical temperature (T_c). The effect of reorientation during the loading and unloading processes can be defined as pseudoelastic behavior. Such behavior has been witnessed in Pd nanowires as shown in Fig. 7b. Such behavior that is unique to the FCC nanowires suggests that the nanowire is highly ductile with the fracture strains of approximately 52%, which seems to be significantly high compared with the fracture strain of bulk FCC metals, which is usually less than 15%. In addition, the recoverable strain can be up to 50%, compared with only 0.5% for most bulk metals. This interesting phenomenon of pseudoelastic behavior has been observed in various FCC MNWs.^{36–38,41,64,67–69}

The schematic explaining the SME is also depicted in Fig. 8. Followed by the lattice orientation of nanowire from $\langle 110 \rangle / [111]$ to $\langle 100 \rangle / [100]$ upon loading, the reverse lattice reorientation occurs only above a size-dependent critical temperature T_c . If unloading takes place at temperatures

below T_c , the reverse lattice reorientation does not occur and the wire retains the $\langle 100 \rangle / [100]$ configuration. On subsequent heating above T_c , the unloaded $\langle 100 \rangle / [100]$ wire spontaneously returns to its original $\langle 110 \rangle / [111]$ configuration through the reverse lattice reorientation. This is a one-way SME that has the $\langle 110 \rangle / [111]$ wire configuration as the parent state. The temperature-dependent feature is also observed in the FCC-to-BCT phase transformation but occurs only when the temperature is above a critical value.³⁸ This is a novel SME driven by surface stress and the high surface-to-volume ratio of MNWs. SME in FCC MNWs causes a recoverable strain up to 50%, which is significantly high compared with 5% to 8% recoverable strain for most bulk SM alloys.

COMPARISON OF FCC MNWs WITH HCP AND BCC MNWs

Compared with FCC MNWs, studies related to HCP and body-centered cubic (BCC) structured nanowires are limited. Magnesium (Mg) and titanium (Ti) are examples of HCP-structured, and iron (Fe) and molybdenum (Mo) are examples of BCC-structured nanowires.

Deformation in HCP materials is driven by complex mechanisms, not clearly understood by the current dislocation theories in experimental and simulation studies.⁷⁰ MD simulations have shown that the deformation mechanism of HCP metals is related to slip–twin interactions.⁷¹ Twinning is a progressive burst of the partial dislocations that reorient the HCP structure into a different crystallographic orientation by forming mirror symmetry with the parent structure. An example of twin boundaries generated during tensile loading of HCP magnesium (Mg) nanowires is depicted in Fig. 9. Twinning in HCP materials is much more complicated in comparison with that of FCC materials. For example, $\{10\bar{1}2\}$ twins in the HCP materials have six variants that can uniquely reorient the parent

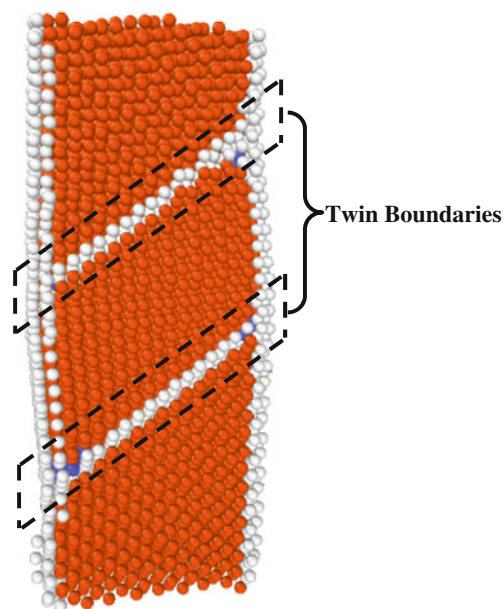


Fig. 9. Twin boundaries generated during the tensile loading of HCP Mg nanowires.

lattice; however, their parameters may or may not obey the Schmid's law.^{72,73} Significant effort had been made to provide a description for the mechanism of twinning nucleation and growth, both in HCP polycrystals and in single crystals.^{74–79} One intriguing aspect is that the twin boundaries generated during deformation harden the material because they impede the dislocation motion^{74,80}; however, during the generation of twins, the crystal structure reorients and thus changes the ability of the dislocations to move, which can lead to softening.⁸¹ Thus, twinning can be used to fine-tune the mechanical properties to achieve an optimal value of strength and ductility.

Mg is among the most widely studied HCP metals because of its lightweight and diverse applications. In Mg with smaller grain size (submicron), ordinary dislocation plasticity may dominate twinning. Dense arrays of twinned regions are considered to be very difficult to produce because of the high twin boundary energy.⁸² However, in contradiction, Yu et al.⁸¹ observed the fundamental embryonic structure of twinning to be dominant in single-crystal Mg nanowire by experimental and simulation studies under various modes of mechanical testing. The formation of the dense nano-twin arrays was also found to be kinetically favorable during their nucleation stage, even in materials with high twin boundary energy such as Mg. Such an understanding of the kinetic nucleation mechanism of deformation twinning may lead to future development of advanced structural materials.

Besides the study of mechanical properties and underlying mechanisms involved in HCP nanowires, the structural stability of HCP Zr nanowire is also investigated by MD simulation.⁸² It is found

that, unlike in the bulk material, an inverse martensitic transformation can occur for an initially $\langle 1100 \rangle$ oriented HCP Zr nanowires into BCC structure at low temperatures, which is driven by the reduction in the nanowire surface energy. The metastable BCC domains subsequently become distorted and transform into a new $\langle 11\bar{2}0 \rangle$ oriented HCP domain, leading to reorientation of the whole nanowire. This behavior has implications for the study of structural transformations at the nano-scale.

MD simulation studies are limited in investigating the mechanical properties of BCC MNWs. One reason is that the deformation mechanisms are not well understood even in bulk BCC metals. Recently, Cao found pseudoelasticity in BCC nanowires that is similar to that in FCC nanowires by using MD simulation and ab initio calculations.⁸³ An initial wire with a $\langle 100 \rangle$ axis and $\{100\}$ side surface has been transformed into a new configuration with a $\langle 110 \rangle$ axis and $\{111\}$ side surface under uniaxial tensile loading. The loaded wire spontaneously transforms back to the original crystal orientation upon unloading, giving rise to about 41% recoverable strain. The primary deformation mechanism associated with the reversible lattice reorientation are twinning and detwinning through twin boundary migration on adjacent $\{112\}$ slip planes. It is further revealed that the physics underlying the novel behavior in these BCC nanowires is the high propensity for twinning and detwinning, which is characterized as the small ratio of twin boundary migration energy to twin boundary formation energy.⁸³ Recently Li et al.⁸⁴ performed MD simulations on BCC polycrystalline molybdenum (Mo) nanowires. They reported that the tensile ductility of the nanowire increases significantly with strain rate and found phase transformation from BCC to either FCC or HCP crystal structure during deformation process.

SUMMARY

Nanowires have been contributing to advancing nanotechnology fields because these low-dimensional structures exhibit great promise as building blocks in nanoscale structures.⁸⁵ MNWs have been the focus of research during the last two decades as a result of their excellent physical and mechanical properties compared with their bulk counterparts, including high stiffness and yield/fracture stress. Simulations have greatly helped in understanding the deformation mechanisms and in reducing the requirements for experiments. The difficulty in handling the nanowires is among the factors that have resulted in a significant scatter in the reported mechanical properties.^{52,86,87} In addition, dynamic concepts of deformation are often difficult to observe directly during nanoscale experiments. Determination of existence and validity of these concepts has greatly benefited from MD simulation studies.

The increasing availability of powerful computational resources and reliable descriptions of atomic interactions have helped in enhancing the MD simulations to obtain more accurate predictions of mechanical properties and in providing detailed insight into the deformation mechanisms.

Mechanical properties of FCC MNWs are found to be closely related to the strain rate, temperature, and cross-sectional size.^{53–56} Within the strain rates feasible in MD simulation studies, it is found that yield stress and yield strain increased with strain rate. It is found that cross slip is responsible for causing plastic deformation in nanowires with a large cross-sectional area and that crystalline slip is the main deformation mechanism for wires with a small cross-sectional area.^{54,88} It is also shown that smaller cross-section FCC MNWs undergo phase transformation, structural reorientations, pseudoelasticity, and SME.^{36–38,41,64,69} The pseudoelastic effect has also been observed in BCC MNWs.⁸³ Dense nano-twin arrays that are very difficult to produce as a result of high twin boundary energy were observed in HCP Mg nanowires.⁸¹ HCP Zr nanowires were found to undergo inverse martensitic transformation into BCC structure at low temperatures as a result of the reduction of nanowire surface energy.⁸²

Significant progress has been made in the computational study of MNW structures and properties as evidenced from the discussion. Advancements in computational technologies, development of more efficient algorithms, and availability of experimental data as input for simulations and for validation of results will drive the further advancements in this field to help obtain results at lower strain rates, using larger simulation cell sizes, and thorough understanding of deformation.

ACKNOWLEDGEMENTS

This work is partly supported by the Office of Naval Research under Grant N00014-10-1-0988 with Dr. Yapa D.S. Rajapakse as the program manager. Dr. Dorel Moldovan from Louisiana State University and Dr. Rakesh Behera from Georgia Institute of Technology are acknowledged for their constructive suggestions.

REFERENCES

1. M. Dresselhaus, Y.-M. Lin, O. Rabin, M. Black, G. Dresselhaus, *Springer Handbook of Nanotechnology*, ed. B. Bhushan (Berlin, Heidelberg: Springer, 2004), pp. 99–146.
2. C.M. Leiber and Z.L. Wang, *MRS Bull.* 32, 99 (2007).
3. Y. Xia, P. Yang, Y. Sun, Y. Wu, B. Mayers, B. Gates, Y. Yin, F. Kim, and H. Yan, *Adv. Mater.* 15, 353 (2003). doi: [10.1002/adma.200390087](https://doi.org/10.1002/adma.200390087).
4. H.S. Park, W. Cai, H.D. Espinosa, and H. Huang, *MRS Bull.* 34, 178 (2009).
5. R.C. Cammarata, *Prog. Surf. Sci.* 46, 1 (1994). doi: [10.1016/0079-6816\(94\)90005-1](https://doi.org/10.1016/0079-6816(94)90005-1).
6. Q.S. Chang, B.K. Tay, X.T. Zeng, S. Li, T.P. Chen, Z. Ji, H.L. Bai, and E.Y. Jiang, *J. Phys.: Condens. Matter* 14, 7781 (2002).
7. J. Wan, Y.L. Fan, D.W. Gong, S.G. Shen, and X.Q. Fan, *Model. Simul. Mater. Sci. Eng.* 7, 189 (1999).
8. R. Agrawal, B. Peng, E.E. Gdoutos, and H.D. Espinosa, *Nano Lett.* 8, 3668 (2008). doi: [10.1021/nl801724b](https://doi.org/10.1021/nl801724b).
9. A. Christ, T. Zentgraf, J. Kuhl, S.G. Tikhodeev, N.A. Gippius, and H. Giessen, *Phys. Rev. B* 70, 125113 (2004).
10. J. Bürki, C.A. Stafford, and D.L. Stein, *Phys. Rev. Lett.* 95, 090601 (2005).
11. A. Bietsch and B. Michel, *Appl. Phys. Lett.* 80, 3346 (2002).
12. B.A. Glavin, *Phys. Rev. Lett.* 86, 4318 (2001).
13. S. Iijima and L.-C. Qin, *Science* 296, 611 (2002). doi: [10.1126/science.296.5568.611a](https://doi.org/10.1126/science.296.5568.611a).
14. M. Kawamura, N. Paul, V. Cherepanov, and B. Voigtländer, *Phys. Rev. Lett.* 91, 096102 (2003).
15. Y. Kondo and K. Takayanagi, *Science* 289, 606 (2000). doi: [10.1126/science.289.5479.606](https://doi.org/10.1126/science.289.5479.606).
16. N.A. Melosh, A. Boukai, F. Diana, B. Gerardot, A. Badolato, P.M. Petroff, and J.R. Heath, *Science* 300, 112 (2003). doi: [10.1126/science.1081940](https://doi.org/10.1126/science.1081940).
17. N. Agraït, G. Rubio, and S. Vieira, *Phys. Rev. Lett.* 74, 3995 (1995).
18. D. Brown and J.H.R. Clarke, *Macromolecules* 24, 2075 (1991). doi: [10.1021/ma00008a056](https://doi.org/10.1021/ma00008a056).
19. C.F. Fan, T. Cagin, Z.M. Chen, and K.A. Smith, *Macromolecules* 27, 2383 (1994). doi: [10.1021/ma00087a004](https://doi.org/10.1021/ma00087a004).
20. D. Rigby and R.J. Roe, *Macromolecules* 23, 5312 (1990). doi: [10.1021/ma00228a002](https://doi.org/10.1021/ma00228a002).
21. G. Schmidt and M.M. Malwitz, *Curr. Opin. Colloid Interface Sci.* 8, 103 (2003). doi: [10.1016/s1359-0294\(03\)00008-6](https://doi.org/10.1016/s1359-0294(03)00008-6).
22. D. Bassolino, H. Alper, and T.R. Stouch, *Drug Des. Discov.* 13, 135 (1996).
23. D. Bemporad, C. Luttmann, and J.W. Essex, *Biophys. J.* 87, 1 (2004).
24. B. Nagireddy and Y.J. Lin, *ASME Conf. Proc.* 2009, 301 (2009).
25. D. Pinisetty, D. Moldovan, and R. Devireddy, *Ann. Biomed. Eng.* 34, 1442 (2006). doi: [10.1007/s10439-006-9148-y](https://doi.org/10.1007/s10439-006-9148-y).
26. R.W. Tejwani, “Experimental and Molecular Dynamics Simulation Studies of Partitioning and Transport Across Lipid Bilayer Membranes” (Ph.D. thesis, Pharmacy University of Kentucky, Lexington, KY, 2009).
27. L. Dai, W.C.D. Cheong, C.H. Sow, C.T. Lim, and V.B.C. Tan, *Langmuir* 26, 1165 (2009). doi: [10.1021/la9022739](https://doi.org/10.1021/la9022739).
28. G. Julien, G. Julien, and B. Sandrine, *Model. Simul. Mater. Sci. Eng.* 19, 074003 (2011).
29. K. Kang and W. Cai, *Philos. Mag.* 87, 2169 (2007).
30. J.D. Monk, “Study of Nanowires Using Molecular Dynamics Simulations” (Ph.D. thesis, Virginia Polytechnic Institute and State University, Blacksburg, VA, 2007).
31. S.J.V. Frankland, V.M. Harik, G.M. Odegard, D.W. Brenner, and T.S. Gates, *Compos. Sci. Technol.* 63, 1655 (2003). doi: [10.1016/s0266-3538\(03\)00059-9](https://doi.org/10.1016/s0266-3538(03)00059-9).
32. P.-H. Lin and R. Khare, *Macromolecules* 42, 4319 (2009). doi: [10.1021/ma9004007](https://doi.org/10.1021/ma9004007).
33. V. Varshney, S.S. Patnaik, A.K. Roy, and B.L. Farmer, *Macromolecules* 41, 6837 (2008). doi: [10.1021/ma801153e](https://doi.org/10.1021/ma801153e).
34. R. Zhu, E. Pan, and A.K. Roy, *Mater. Sci. Eng. A* 447, 51 (2007). doi: [10.1016/j.msea.2006.10.054](https://doi.org/10.1016/j.msea.2006.10.054).
35. G.D. Smith, D. Bedrov, L. Li, and O. Bytner, *J. Chem. Phys.* 117, 9478 (2002). http://www.nature.com/nmat/journal/v2/n10/supinfo/nmat977_S1.html.
36. J. Diao, K. Gall, and M.L. Dunn, *Nat. Mater.* 2, 656 (2003).
37. J. Diao, K. Gall, and M.L. Dunn, *Phys. Rev. B* 70, 075413 (2004).
38. J. Lao and D. Moldovan, *Appl. Phys. Lett.* 93, 093108 (2008).
39. W. Liang and M. Zhou, *Phys. Rev. B* 73, 115409 (2006).
40. W. Liang, M. Zhou, and F. Ke, *Nano Lett.* 5, 2039 (2005). doi: [10.1021/nl0515910](https://doi.org/10.1021/nl0515910).
41. H.S. Park, K. Gall, and J.A. Zimmerman, *Phys. Rev. Lett.* 95, 255504 (2005).
42. D. Frenkel and B. Smit, *Understanding Molecular Simulation: From Algorithms to Applications* (Atlanta, GA: Academic Press, 2001).
43. M.S. Daw and M.I. Baskes, *Phys. Rev. Lett.* 50, 1285 (1983).
44. M.S. Daw, S.M. Foiles, and M.I. Baskes, *Mater. Sci. Rep.* 9, 251 (1993). doi: [10.1016/0920-2307\(93\)90001-u](https://doi.org/10.1016/0920-2307(93)90001-u).
45. M.I. Baskes, *Phys. Rev. B* 46, 2727 (1992).
46. E.Z. da Silva, A.J.R. da Silva, and A. Fazzio, *Phys. Rev. Lett.* 87, 256102 (2001).

47. J. Diao, K. Gall, M.L. Dunn, and J.A. Zimmerman, *Acta Mater.* 54, 643 (2006). doi:[10.1016/j.actamat.2005.10.008](https://doi.org/10.1016/j.actamat.2005.10.008).
48. K. Gall, J. Diao, and M.L. Dunn, *Nano Lett.* 4, 2431 (2004). doi:[10.1021/nl048456s](https://doi.org/10.1021/nl048456s).
49. S.J.A. Koh and H.P. Lee, *Nanotechnology* 17, 3451 (2006).
50. W. Liang, D.J. Srolovitz, and M. Zhou, *J. Mech. Phys. Solids* 55, 1729 (2007). doi:[10.1016/j.jmps.2007.01.001](https://doi.org/10.1016/j.jmps.2007.01.001).
51. H.S. Park, K. Gall, and J.A. Zimmerman, *J. Mech. Phys. Solids* 54, 1862 (2006). doi:[10.1016/j.jmps.2006.03.006](https://doi.org/10.1016/j.jmps.2006.03.006).
52. B. Wu, A. Heidelberg, and J.J. Boland, *Nat. Mater.* 4, 525 (2005). http://www.nature.com/nmat/journal/v4/n7/suppinfo/nmat1403_S1.html.
53. S.J.A. Koh, H.P. Lee, C. Lu, and Q.H. Cheng, *Phys. Rev. B* 72, 085414 (2005). doi:[10.1080/14786430701280943](https://doi.org/10.1080/14786430701280943).
54. W. Liang and M. Zhou, *Proc. Inst. Mech. Eng. C* 218, 599 (2004). doi:[10.1016/j.commatsci.2007.05.012](https://doi.org/10.1016/j.commatsci.2007.05.012).
55. H.S. Park and J.A. Zimmerman, *Phys. Rev. B* 72, 054106 (2005). doi:[10.1016/j.commatsci.2009.02.015](https://doi.org/10.1016/j.commatsci.2009.02.015).
56. H.A. Wu, A.K. Soh, X.X. Wang, and Z.H. Sun, *Key Eng. Mater.* 261, 33 (2004).
57. Y.-H. Wen, Z.-Z. Zhu, and R.-Z. Zhu, *Comput. Mater. Sci.* 41, 553 (2008). doi:[10.1243/095440604774202231](https://doi.org/10.1243/095440604774202231).
58. A. Cao and E. Ma, *Acta Mater.* 56, 4816 (2008).
59. E. Rabkin, H.S. Nam, and D.J. Srolovitz, *Acta Mater.* 55, 2085 (2007).
60. H.A. Wu, *Mech. Res. Commun.* 33, 9 (2006). doi:[10.1016/j.actamat.2008.05.044](https://doi.org/10.1016/j.actamat.2008.05.044).
61. P.Z. Coura, S.B. Legoas, A.S. Moreira, F. Sato, V. Rodrigues, S.O. Dantas, D. Ugarte, and D.S. Galvão, *Nano Lett.* 4, 1187 (2004). doi:[10.1016/j.actamat.2006.10.058](https://doi.org/10.1016/j.actamat.2006.10.058).
62. E.B. Tadmor and N. Bernstein, *J. Mech. Phys. Solids* 52, 2507 (2004). doi:[10.1016/j.mechrescom.2005.05.012](https://doi.org/10.1016/j.mechrescom.2005.05.012).
63. C.R. Weinberger and W. Cai, *J. Mater. Chem.* 22, 3277 (2012). doi:[10.1016/j.actamat.2006.02.006](https://doi.org/10.1016/j.actamat.2006.02.006).
64. K. Gall, J. Diao, M.L. Dunn, M.I. Haftel, N. Bernstein, and M.J. Mehl, *J. Eng. Mater. Technol.* 127, 417 (2005). doi:[10.1021/nl049725h](https://doi.org/10.1021/nl049725h).
65. O. Gülseren, F. Ercolessi, and E. Tosatti, *Phys. Rev. Lett.* 80, 3775 (1998). doi:[10.1016/j.jmps.2004.05.002](https://doi.org/10.1016/j.jmps.2004.05.002).
66. M.I. Haftel and K. Gall, *Phys. Rev. B* 74, 035420 (2006).
67. H.S. Park and C. Ji, *Acta Mater.* 54, 2645 (2006).
68. C. Ji and H.S. Park, *J. Comput. Theor. Nanosci.* 4, 578 (2007).
69. W. Liang and M. Zhou, *J. Eng. Mater. Technol.* 127, 423 (2005).
70. C.D. Barrett, M.A. Tschopp, and H. El Kadiri, *Scripta Mater.* 66, 666 (2012).
71. G.P. Zheng, Y.M. Wang, and M. Li, *Acta Mater.* 53, 3893 (2005). doi:[citeulike-article-id:4387623](https://doi.org/citeulike-article-id:4387623).
72. V. Yamakov, D. Wolf, S.R. Phillpot, A.K. Mukherjee, and H. Gleiter, *Nat. Mater.* 3, 43 (2004). doi:[10.1016/j.scripamat.2012.01.034](https://doi.org/10.1016/j.scripamat.2012.01.034).
73. Y. Zhu, X. Liao, and X. Wu, *JOM* 60 (9), 60 (2008). doi:[10.1016/j.actamat.2005.04.038](https://doi.org/10.1016/j.actamat.2005.04.038).
74. O. Bouaziz, S. Allain, and C. Scott, *Scripta Mater.* 58, 484 (2008).
75. H. El Kadiri and A.L. Oppedal, *J. Mech. Phys. Solids* 58, 613 (2010). doi:[10.1007/s11837-008-0120-1](https://doi.org/10.1007/s11837-008-0120-1).
76. D. Kuhlmann-Wilsdorf, *Phys. Status Solidi A* 47, 639 (1978). doi:[10.1016/j.scripamat.2007.10.050](https://doi.org/10.1016/j.scripamat.2007.10.050).
77. N. Munroe, X. Tan, and H. Gu, *Scripta Mater.* 36, 1383 (1997). doi:[10.1016/j.jmps.2009.12.004](https://doi.org/10.1016/j.jmps.2009.12.004).
78. H. Van Swygenhoven, P.M. Derlet, and A.G. Froseth, *Nat. Mater.* 3, 399 (2004). doi:[10.1002/pssa.2210470235](https://doi.org/10.1002/pssa.2210470235).
79. M.H. Yoo, *Metall. Trans. A* 12A, 409 (1981). doi:[10.1016/s1359-6462\(97\)00048-1](https://doi.org/10.1016/s1359-6462(97)00048-1).
80. X.L. Wu, K.M. Youssef, C.C. Koch, S.N. Mathaudhu, L.J. Kecskés, and Y.T. Zhu, *Scripta Mater.* 64, 213 (2011).
81. Q. Yu, L. Qi, K. Chen, R.K. Mishra, J. Li, and A.M. Minor, *Nano Lett.* 12, 887 (2012).
82. S. Li, X. Ding, J. Li, X. Ren, J. Sun, E. Ma, and T. Lookman, *Phys. Rev. B* 81, 245433 (2010). doi:[10.1016/j.scripamat.2010.10.024](https://doi.org/10.1016/j.scripamat.2010.10.024).
83. A. Cao, *J. Appl. Phys.* 108, 113531 (2010).
84. X. Li, W. Hu, S. Xiao, and W.-Q. Huang, *Physica E* 43, 1131 (2011).
85. C.M. Leiber, *MRS Bull.* 28, 486 (2003).
86. A. Heidelberg, L.T. Ngo, B. Wu, M.A. Phillips, S. Sharma, T.I. Kamins, J.E. Sader, and J.J. Boland, *Nano Lett.* 6, 1101 (2006). doi:[10.1016/j.physe.2011.01.017](https://doi.org/10.1016/j.physe.2011.01.017).
87. E.C.C.M. Silva, L. Tong, S. Yip, and K.J. Van Vliet, *Small* 2, 239 (2006).
88. C. Ji and H.S. Park, *Appl. Phys. Lett.* 89, 181916 (2006). doi:[10.1021/nl060028u](https://doi.org/10.1021/nl060028u).
89. W. Liang and M. Zhou, *Philos. Mag.* 87, 2191 (2007). doi:[10.1002/sml.200500311](https://doi.org/10.1002/sml.200500311).
90. Z. Yang, Z. Lu, and Y.-P. Zhao, *Comput. Mater. Sci.* 46, 142 (2009).